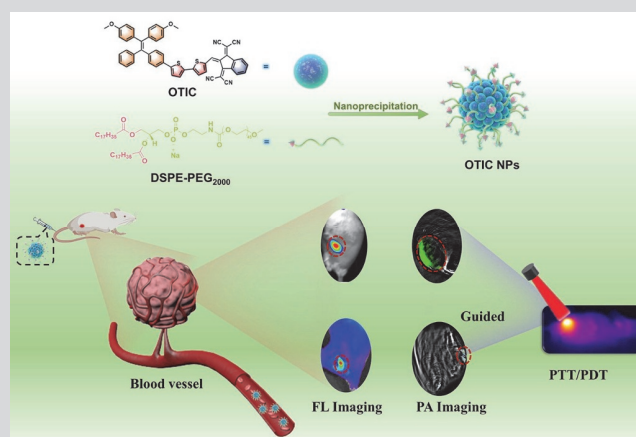# Aggregation-induced Emission Probe for Fluorescence/ Photoacoustic Dual-modality Imaging and Photodynamic/Photothermal Treatment

CHEN Peiyu, ZHANG Guoyang, LI Jiguang, MA Lijun, ZHOU Jiaying, ZHU Mingguang, LI Shuo✉ and WANG Zhuo✉

The combination of near-infrared (NIR) fluorescence imaging (FLI) and photoacoustic imaging (PAI) can effectively compensate for each other's inherent limitations, which can provide reliable and rich information on tumor biology. Therefore, the development of FL/PA dual-modality imaging probes is beneficial for achieving precision cancer diagnosis and treatment. Herein, we designed an efficient phototherapy agent methoxy bithiophene indene (OTIC), which was based on aggregation-induced emission (AIE) active fluorophores. To improve the water dispersion and enrichment of OTIC at the tumor site, OTIC nanoparticles (OTIC NPs) were prepared by a nanoprecipitation method. The balance between radiation and non-radiation energy dissipation was regulated by the strong donor-acceptor interaction and intramolecular motion. So OTIC NPs exhibited bright NIR fluorescence, photoacoustic signals, efficient generation of reactive oxygen species, and high photothermal conversion efficiency under NIR irradiation. Accurate imaging of the tumor and mice sentinel lymph nodes (SLNs) with OTIC NPs was visualized by NIR FL/PA dual-modal imaging. With the comprehensive imaging information provided by OTIC NPs *in vivo*, tumors were ablated under laser irradiation, which greatly improved the therapeutic efficacy. OTIC NPs would be possible to realize the precise guidance of FL/PA imaging for tumor treatment in the future clinical application.

1 Introduction

Multimodal imaging integrates two or more imaging modalities to realize the accurate and selective imaging activity.[1−4] In recent years, the combination of multimodal imaging and phototherapy has been used for the treatment of tumors. The imaging-guided therapy has the advantages, such as real-time monitoring, multi-functions in one platform, and saving time for diagnosis and treatment.[5−8] Fluorescence signals are obtained by capturing the surface of the tumor tissue under excitation, so the main limitation of fluorescence imaging (FLI) is the shallow tissue penetration depth of light.[9−11] Photoacoustic imaging (PAI) provides deep tissue imaging with rich optical contrast and high depth resolution.[12,13] When the PA contrast agent is excited by the pulsed laser, the energy is released in the form of heat and generates local thermoelastic expansion. The repeated excitation of the pulsed laser causes pressure fluctuations, which propagate through the tissue to produce detectable ultrasound.[14,15] Near-infrared fluorescence imaging (NIR FLI) shows some advantages in reducing the influence of auto-fluorescence and improving the signal-noise ratio (SNR).[16−18] Dual-mode imaging provides reliable and rich information on tumor biology, and improves the accuracy of cancer diagnosis. Therefore, the combination of FLI and PAI can effectively compensate for the inherent limitations of each other and realize the accurate imaging.

Phototherapy has attracted attention for its high selectivity, noninvasiveness, precise controllability and negligible resistance.[19−23] Photodynamic therapy (PDT) kills cancer cells indirectly by the formation of reactive oxygen species (ROS).[24−27] The PDT process can affect the intracellular metabolism, damage the cell structure and inactivate cellular proteins, thereby killing malignant tumor

✉ WANG Zhuo
wangzhuo77@mail.buct.edu.cn
✉ LI Shuo
2020400223@mail.buct.edu.cn
State Key Laboratory of Chemical Resource Engineering, College of Chemistry, Beijing Advanced Innovation Center for Soft Matter Science and Engineering, Beijing University of Chemical Technology, Beijing 100029, P. R. China

cells.[28−30] Photothermal therapy (PTT) relies on materials with photothermal effects to convert light to heat, which relaxes cell membranes and denatures proteins, killing cancer cells in an irreversible manner.[31−35] Collaboration of PDT and PTT is a novel strategy to overcome respective shortcomings and improve therapeutic effect.[36,37] The development of all-in-one phototherapeutic agents that combine multimodal imaging with PDT and PTT remains challenging.

According to the Jablonski diagram, the energy of the excited state is dissipated through both radiative and nonradiative pathways. The dissipated energy of radiative decay is available for FLI, and the nonradiative decay fraction provides feasibility for PAI, photothermal imaging (PTI), PTT, and PDT.[38−41] The electronic transition of chemical structure spontaneously favors either radiative or nonradiative pathways. In this case, the effect of phototherapy can be tuned by modulating the balance between radiative and nonradiative energy dissipation. The number of free-moving molecular rotors and oscillators in aggregate induced emission luminogens (AIEgens) can affect the nonradiative transitions by changing the intra-molecular motion, thus balancing the radiative and nonradiative transitions.[42−45] Typically, a highly distorted tetraphenylethylene (TPE) group with four benzene rings ensures intramolecular motility.[46] The electron donor-acceptor (D-A) interactions can significantly promote the bathochromic shift of absorption/emission and ROS production due to the reduced electronic band gap and facilitated intersystem crossing (ISC) process.[47−49] The structure of molecules can realize multi-functions by linkage of different chemical groups.[50,51]

In this work, we developed a D-A structured molecule methoxy bithiophene indene (OTIC), which achieved FLI/PAI guided PTT and PDT synergistic therapy. To improve water solubility and biocompatibility of OTIC, OTIC nanoparticles (OTIC NPs) were prepared by nanoprecipitation method, which facilitated the aggregation of OTIC at the tumor site through the enhanced permeability and retention (EPR) effect, thereby improving the accuracy of dual-mode imaging. Under the laser irradiation, OTIC NPs have stable photothermal performance with a photothermal conversion efficiency (PCE) of 30% and excellent ROS production capacity. The fluorescence quantum yield (QY) of OTIC NPs is up to 1.5% with Cy5 as the reference (QY=0.2%). The FLI/PAI ability of OTIC NPs was demonstrated with 4T1 tumor-bearing mice and sentinel lymph node tumor model.[52−55] The dual-modality imaging with high sensitivity and spatial resolution *in vivo* provided a good guidance in the diagnosis and treatment of tumors. The antitumor treatment experiments also showed that OTIC NPs had good tumor ablation. OTIC NPs present potentials to realize FLI and PAI-guided PTT-PDT synergistic therapy and open new perspectives for the development of the therapeutic systems.

2 Experimental

2.1 Materials and Instruments

The solvents were purified by standard methods. The chemical reagents were obtained from commercial resources and utilized as is. All the experimental water was deionized (DI). 4,4'-Dimethoxybenzophenone and 4-bromobenzophenone were purchased from Beijing Inno-chem Technology Co., Ltd. (Beijing, China). Anhydrous potassium carbonate was purchased from Fuchen (Tianjin) Chemical Reagent Co., Ltd. (Tianjin, China). Zinc powder was purchased from Sinopharm Group Chemical Reagent Co., Ltd. Tetrakis(triphenylphosphine) palladium(0) and titanium tetrachloride were purchased from Shanghai Aladdin Bio-chemical Technology Co., Ltd. (Shanghai, China). [1,1'-Bis(diphenylphosphino)ferrocene] dichloropalladium(II), bis(pinacolato)-diboron, potassium acetate, 5-bromo-2,2'-bithiophene-5'-carboxaldehyde and 1,3-bis (dicyano-methylidene) indan were purchased from Shanghai TCI Chemical Industry Development Co., Ltd. (Shanghai, China). Nuclear magnetic resonance (NMR) spectra were recorded on an AVANCE III HD 400 (400 MHz, Switzerland) spectrometer in CDCl₃ or DMSO-d₆ solutions at room temperature. UV-Vis spectra were recorded on a UV-Vis spectrophotometer (Hitachi, U-3900H, Japan). Fluorescence spectra were recorded on a fluorescence spectrophotometer (Hitachi, F-4600, Japan). Mass spectra results were obtained from the Beijing Mass Spectrometry Center, Institute of Chemistry, Chinese Academy of Sciences. A transmission electron microscope (Hitachi HT7700, Japan) was used to characterize the particle size of nanoparticles. Confocal laser scanning microscope (CLSM, Lecia SP8, Germany) was used for cell imaging. Zetasizer Nano (ZS90, UK) was used to test the hydrated particle size of nanoparticles. A 660 nm laser was obtained by laser device (RAL660T1-2.0 W, Beijing, China). PA imaging was acquired on the multispectral optical tomography system (MSOT in Vision 256, iThera Medical, Germany, ViewMSOT 4.0). FL imaging was acquired on the *in vivo* imaging system (IVIS Spectrum, PerkinElmer, USA, Living Image 4.4).

2.2 Synthesis of OTIC

2.2.1 Synthesis of Compound 1

(i) In a 250 mL round-bottom double necked flask, 4,4'-dimethoxybenzophenone (5.22 g, 20.0 mmol), 4-bromobenzophenone (4.85 g, 20.0 mmol), and zinc powder

(10.5 g, 160 mmol) were dissolved in 100 mL of degassed tetrahydrofuran. The reaction was placed in an acetone bath, and TiCl$_4$ (8.8 mL, 80 mmol) was slowly added dropwise with a syringe in 30 min. After refluxing at 80 °C for 8 h under a nitrogen atmosphere, the saturated K$_2$CO$_3$ solution (100 mL) was added dropwise to the beaker, and a solid was precipitated, which was filtered through celite under reduced pressure, washed with dichloromethane, and the filtrate was collected. The filtrate was extracted three times with dichloromethane, the extract was dried over anhydrous sodium sulfate, and then the solvent was removed by rotary evaporation under reduced pressure. Finally, a yellow solid was obtained through column chromatography [V(petroleum)/V(ethyl acetate)=20:1] (3.45 g, 36.6%).¹H NMR (400 MHz, CDCl$_3$), δ: 7.26 (d, J=7.7 Hz, 2H), 7.13 (s, 3H), 7.05 (s, 2H), 7.01—6.85 (m, 6H), 6.69 (dd, J=13.3, 8.3 Hz, 4H), 3.78 (d, J=10.6 Hz, 6H).

(ii) In a 100 mL round-bottom double necked flask, product of compound **1** (0.5 g, 1.05 mmol), bis(pinacolato)-diboron (0.4 g, 1.6 mmol), potassium acetate (0.31 g, 3.15 mmol) and [1,1'-bis(diphenylphosphino)ferrocene]-dichloropalladium (II) PdCl$_2$ (dppf) (70 mg, 0.096 mmol) were dissolved in 30 mL of 1,4-dioxane. After refluxing at 110 °C for 8 h under a nitrogen atmosphere, the reaction was cooled to room temperature, the reaction solution was extracted with dichloromethane, the extract was dried over anhydrous sodium sulfate, and then the solvent was removed by rotary evaporation under reduced pressure. Finally, a yellow solid was obtained through column chromatography [V(Petroleum)/V(ethyl acetate)= 10:1] (0.35 g, 63.6%). ¹H NMR (400 MHz, CDCl$_3$), δ: 7.56 (d, J=8.1 Hz, 2H), 7.11 (d, J=7.1 Hz, 3H), 7.07—7.01 (m, 4H), 6.96 (dd, J=8.7, 1.3 Hz, 4H), 6.68—6.63 (m, 4H), 3.76 (d, J=2.6 Hz, 6H), 1.35 (s, 12H).

2.2.2 Synthesis of Compound 2

In a 100 mL round-bottom double necked flask, compound **1** (0.1 g, 0.19 mmol), 5-bromo-2,2'-bithiophene-5'-carboxaldehyde (44 mg, 0.16 mmol), and tetrakis (triphenylphosphine) palladium(0) [Pd(PPh$_3$)$_4$] (5.0 mg, 0.004 mmol) were dissolved in 30 mL of DMF. The reaction was heated to 140 °C, and an appropriate amount of potassium carbonate solution (2 mol/L) was injected and refluxed for 6 h. After the reaction was cooled to room temperature, the reaction solution was extracted with di-chloromethane, and the extract was dried with anhydrous sodium sulfate, and then the solvent was removed by rotary evaporation under reduced pressure. Finally, an orange solid was obtained through column chromatography [V(petroleum)/V(dichloromethane)=1:1] (75 mg, 66.5%). ¹H NMR (400 MHz, CDCl$_3$)), δ: 9.88 (s, 1H), 7.69 (d, J=4.0 Hz,

1H), 7.38 (d, J=8.3 Hz, 2H), 7.33 (d, J=3.8 Hz, 1H), 7.29—7.22 (m, 2H), 7.15 (q, J=5.9 Hz, 3H), 7.10—7.05 (m, 4H), 6.98 (dd, J=17.8, 8.7 Hz, 4H), 6.68 (dd, J=13.4, 8.7 Hz, 4H), 3.77 (d, J=4.4 Hz, 6H).

2.2.3 Synthesis of OTIC

In a 100 mL round-bottom double necked flask, compound **2** (0.17 g, 0.29 mmol), and 1,3-bis(dicyanomethylidene)indan (70.0 mg, 0.29 mmol) were dissolved in 30 mL of acetic anhydride. The mixture was stirred at 60 °C for 5 h. After evaporation of solvent, the solid residue was washed with n-hexane (5 mL×2) and diethyl ether (5 mL). The resulted solid was further recrystallized from chloroform/n-hexane mixture to give the final black blue solid product OTIC (70.0 mg, 30.4%). ¹H NMR (400 MHz, DMSO-d$_6$), δ: 8.44 (dd, J=5.9, 3.2 Hz, 2H), 8.39 (s, 1H), 8.03—7.96 (m, 3H), 7.71 (d, J=3.9 Hz, 1H), 7.60 (t, J=4.3 Hz, 2H), 7.53 (d, J=8.4 Hz, 2H), 7.15 (d q, J=14.3, 7.0 Hz, 3H), 7.01 (dd, J=8.3, 2.8 Hz, 4H), 6.93 (d, J=8.7 Hz, 2H), 6.87 (d, J=8.7 Hz, 2H), 6.75 (d, J=8.8 Hz, 2H), 6.70 (d, J=8.8 Hz, 2H), 3.69 (d, J=2.7 Hz, 6H). ¹³C NMR (101 MHz, DMSO-d$_6$), δ: 184.21, 161.84, 158.59, 158.41, 158.26, 147.53, 146.28, 144.76, 144.01, 141.01, 138.45, 138.31, 135.98, 135.48, 135.25, 134.31, 133.85, 132.52, 132.13, 131.32, 130.83, 130.56, 129.61, 129.09, 128.42, 126.87, 126.71, 126.04, 125.56, 125.38, 125.28, 122.02, 118.39, 118.29, 114.15, 113.83, 113.63, 103.23, 55.39. MALDI-TOF-MS, m/z, [M]+ calcd: 808.20000; found: 808.19580.

2.3 Preparation of OTIC Nanoparticles

OTIC (1.0 mg) and 1,2-distearoyl-sn-glycero-3-phosphoethanolamine-N-[methoxy(polyethylene glycol)-2000] (DSPE-mPEG2000, 4.0 mg) were respectively dissolved in 1.0 mL of tetrahydrofuran (THF) solution, which was poured to 10 mL of deionized water under sonication for 10 min. Then the mixtures were transferred to a dialysis tube (MWCO 3500 Da) and dialyzed against deionized water for 36 h. To remove THF completely, the water was replaced with fresh water every 4 h. The final obtained nanoparticle solution was freeze-dried or concentrated by ultrafiltration before use.

2.4 Cell Viability Test

The HeLa cells were seeded on 96 well plates in DMEM (with 10% FBS, 1% penicillin/streptomycin) in 5% CO$_2$ at 37 °C in a humidified incubator. Then, the cells in a logarithmic growth phase were harvested and seeded in 96 well plates at a density of 1×10⁴ cells/well for 24 h incubation. Subsequently, the medium was replaced with a fresh medium containing different concentrations of OTIC NPs

(100 μL/well) and cultured together for another 24 h. Cells were then incubated with a fresh MTT solution (50 μL/well). After 4 h, the media was removed and washed with PBS three times. Then 150 μL of DMSO was added to each well to dissolve the formazan. Finally, the absorbance of the products was measured at a wavelength of 490 nm by a microplate reader. The relative cell viability was calculated according to the following formula:

$$\text{Cell viability (\%)} = \frac{OD_{sample} - OD_{background}}{OD_{control} - OD_{background}} \times 100\% \quad (1)$$

2.5 Live/Dead Cell Staining Assay

First, HeLa cells were seeded on a confocal dish at a density of $ca.$ 10^6 cells per well and cultured in an incubator for 24 h. Second, the culture medium was replaced with 20 μg/mL OTIC NPs, and incubated continuously about 12 h under dark condition. Third, the cells were irradiated with 660 nm laser (0.5 W/cm^2) for 3 min, and after the treatment, the cells were further cultured for 4 h. Finally, the cells were rinsed with PBS and stained by 1.0 μmol/L calcein acetoxymethyl ester (Calcein AM) and 1.0 μmol/L propidium iodide (PI) for 30 min, and the residual dyes were washed out by PBS three times. The results of containing were observed by CLSM.

2.6 Animals and Tumor Models

BALB/c nude mice (~ 4 weeks old) were purchased from the Beijing Charles River Laboratory Animal Technology (Beijing, China). All animals were acclimatized to the animal facility for one week prior to experimentation and housed under pathogen-free conditions. All animals were fed under conditions of 25 °C and 55% of humidity. Allowed free access to standard laboratory water and chow. The xenograft tumor models were established by subcutaneous injection of 1×10^7 4T1 cells in PBS buffer to the right flanks of each mouse. After about 10 days, mice with tumor volumes at about 100 mm^3 were used subsequently. Tumor volumes were measured every other day using a caliper and calculated using the following formula:

$$\text{Volume} = \frac{(\text{Tumor length}) \times (\text{Tumor width})^2}{2} \quad (2)$$

Animal studies were approved by the Ethical Committee of China-Japan Friendship Hospital and performed under legal protocols. The approval number is zryhyy12-20-10-2.

2.7 *In vivo* NIR Fluorescence and Photoacoustic Imaging

The 4T1 tumor-bearing mice were administered with OTIC NPs in saline at a dose of 200 μL of OTIC per mouse *via* tail vein. Then, at 4, 8, 16, 24, 36 and 48 h post-injection, the mice were anesthetized using 2% isoflurane in oxygen. Meanwhile, *in vivo* photoacoustic imaging was also carried out on the multispectral optical tomography system at designated time intervals after injection of OTIC NPs. To evaluate the metabolic distributions of OTIC NPs, the mice were sacrificed at 1, 3, 6, 12, 24, 48 h post-injection. Major organs (heart, liver, spleen, lung and kidney) and tumor were excised, followed by washing the surface with saline several times for NIR fluorescence imaging and quantitative analyses by IVIS spectrum.

3 Results and Discussion

3.1 Design and Synthesis of OTIC

As shown in Scheme 1A, the designed compound OTIC included methoxy-tetraphenylethylene (OMe-TPE) unit (D), 1,3-bis(dicyanomethylidene)indane moiety (A), and thiophene segment (D and π-bridge), showed D-A interaction and extended π-conjugation. OMe-TPE moiety was selected as molecular rotors. The highly distorted conformation of TPE segment extends the intermolecular distance and induces relatively loose intermolecular filling even in the aggregated state, which helps to retain part of intramolecular rotation and facilitates the heat generation within the OTIC. The propeller-like twisted structure of the OTIC could efficiently restrain the quenching of fluorescence by significantly reducing the intermolecular π-π stacking. The intramolecular bond stretching vibration as another high frequency molecular motion is less susceptive to the external environmental constraints. Two malononitrile-modified indane was chosen as electronic acceptor. Moreover, the vigorous stretching vibrations of C≡N bonds of OTIC were conducive to the intramolecular motion in aggregate state. The chemical structure of OTIC was constructed with the above groups to endow the intramolecular rotation for PTT-PTI-PAI efficiency. OTIC had AIE properties and longer emission. OTIC was encapsulated with amphiphilic co-polymer DSPE-mPEG2000 for water dispersibility and biocompatibility (Scheme 1B).

3.2 Characterization, Properties of OTIC and OTIC NPs

The properties of OTIC were characterized and further recorded in Fig. 1 and Figs. S1—S6 in the Electronic Supplementary Information (ESI). The maximum absorption peaks of OTIC and OTIC NPs were located at 583 and 635 nm, respectively. The emission spectra of the OTIC were mainly located in the 600—800 nm region. The absorption of OTIC NPs had a redshift of 52 nm compared to OTIC
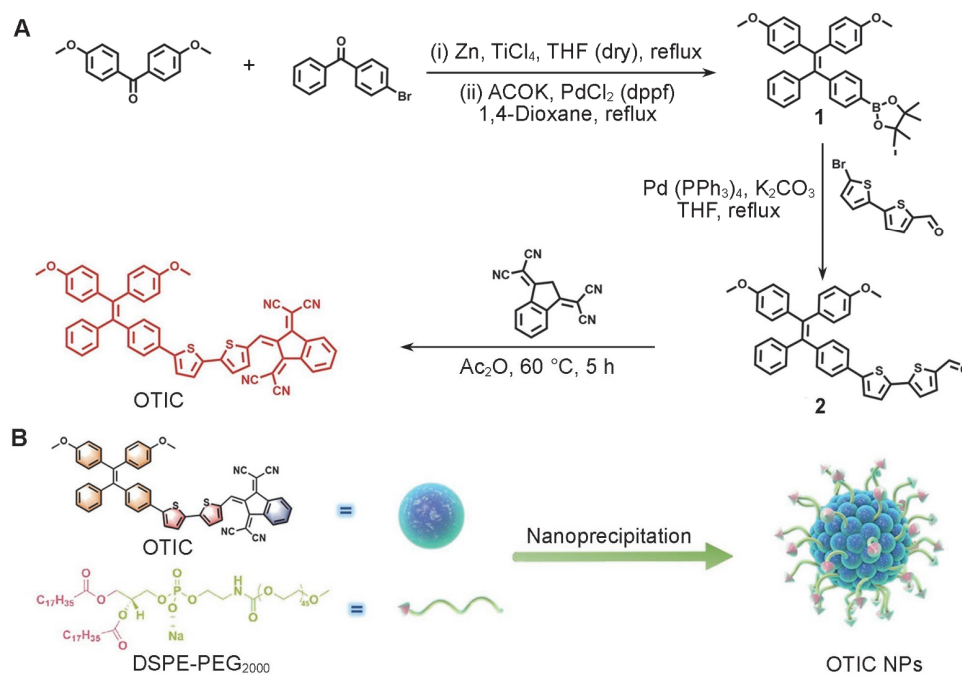
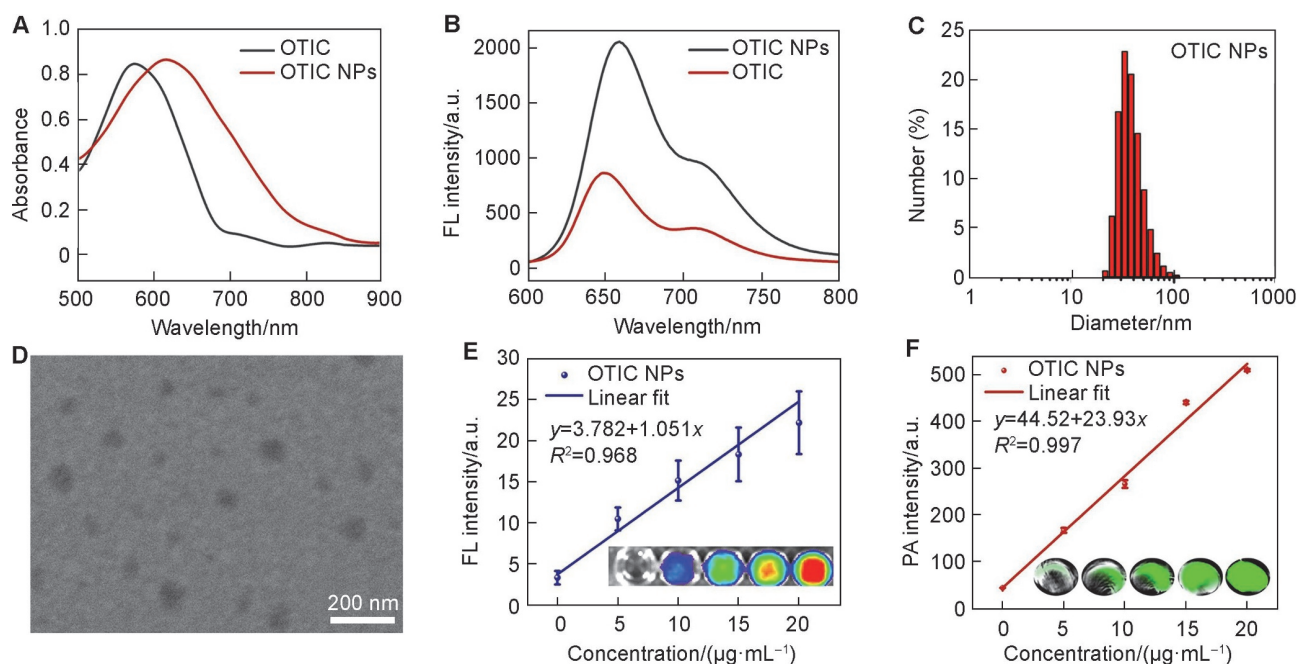**Scheme 1 Synthetic route of OTIC (A) and preparation of OTIC NPs (B)**

Fig. 1 Spectral characterization of OTIC NPs
(A) Absorption spectra of OTIC and OTIC NPs; (B) fluorescence spectra of OTIC and OTIC NPs; (C) DLS data of OTIC NPs; (D) TEM image (scale bar: 200 nm) of OTIC NPs; (E) linear fit of FL intensity and OTIC NPs concentration (inset: FL images of respective concentrations. λ_{ex}: 630 nm; λ_{em}: 640—760 nm); (F) linear fit of PA intensity and OTIC NPs concentration (inset: PA images of respective concentrations).

(Fig. 1A). The possible reason was that the internal stress inside the OTIC NPs increased, which led to a change of the energy band structure.[56] Meanwhile, the fluorescence intensity of OTIC NPs increased compared to OTIC due to the aggregation effect of nanoparticles (Fig. 1B). The AIE features of OTIC were studied in a CHCl₃/hexane solvent system with different hexane fractions. OTIC exhibited weak fluorescence in CHCl₃ solution (Fig. S7 in the ESI), mainly

ascribing to the energy consumption of the excited state dominated by the active intramolecular motions in the solution state. The emission intensities of OTIC raised gradually along with the increasing of hexane in the mixed solvent, which was due to the restriction of intramolecular motion induced by molecular aggregation. Based on the calculation of the highest occupied molecular orbital (HOMO) and the lowest unoccupied molecular orbital

(LUMO) levels, the energy bandgap of OTIC was estimated as 1.78371 eV (Fig. S8 in the ESI). Besides, by encapsulating the prepared OTIC within an amphipathic DSPE-PEG2000 molecule, the corresponding OTIC NPs had a high QY of 1.5% (relative to Cy5 of 0.2%) (Fig. S9 in the ESI). The molar absorption coefficient of OTIC NPs is 4.34×10^4 $mol^{-1} \cdot L \cdot cm^{-1}$. Dynamic light scattering (DLS) measurement revealed that the OTIC NPs had average sizes of about 78.2 nm (Fig. 1C), rightly located in the range of 50—100 nm, which was optimal for tumor accumulation driven by the EPR effect. Transmission electron microscopy (TEM) images revealed uniform circular morphology with diameters of about 45.0 nm for OTIC NPs (Fig. 1D), which was smaller than the hydrodynamic diameter values revealed by DLS, possibly due to the absence of hydration layer on the surface of the NPs. The FLI and PAI capabilities of OTIC NPs were examined with an IVIS spectrum imaging system and a multispectral optoacoustic tomography (MSOT) imaging system, respectively. The fluorescence intensity with the increasing concentration of OTIC NPs was presented in Fig. 1E. The FL signal exhibited a linear correlation with the concentration of OTIC NPs. OTIC NPs were embedded in an artificial agar phantom and imaged in the MSOT system. OTIC NPs showed a PA signal as the concentration of OTIC NPs increased, and there was a good linear relationship between the PA signal and the concentration of OTIC NPs (Fig. 1F). OTIC NPs presented FL/PA imaging ability under different excitation wavelengths and were a great FL/PA dual-modality agent.

3.3 Photodynamic and Photothermal Properties of OTIC and OTIC NPs

The D-π-A structure of OTIC NPs induced the generated ROS for photodynamic therapy. The ROS generation efficiency of OTIC NPs was further evaluated by 2',7'-dichlorodihydrofluorescein diacetate (DCFH-DA) as an indicator. The irreversible reaction between DCFH-DA (no fluorescence) and ROS showed green fluorescence. As illustrated in Fig. 2A, the fluorescence intensity of DCF (2',7'-dichloro-fluorescein, green fluorescence) was rapidly enhanced with a 660 nm laser irradiation in the presence of OTIC NPs, which indicated that OTIC NPs had a high

ROS generation capacity. In the presence of OTIC NPs, the emission intensity of DCFH reached over 50-fold after 2 min laser irradiation. In Fig. S10 in the ESI, with the increase of laser time, the fluorescence intensity of DCF increases, and the rate of ROS of OTIC NPs is 1.6 times that of Chlorin e6 (Ce6, commercial photosensitizer). The indicator 9,10-anthracenediyl-bis(methylene) dimalonic acid (ABDA) for singlet oxygen ($^1O_2$), the indicator dihydrorhodamine123 (DHR123) for superoxide anion (O_2^-) and the indicator tere-phthalic acid (TA) for radical ($\cdot OH$) were utilized to confirm the generation of ROS species by OTIC NPs. In Fig. S11, A—C in the ESI, the spectral change curve of Fig. S11B compared to the Fig. S11A and Fig. S11C was more obvious, so it could be concluded that the type of ROS produced by OTIC NPs was mainly O_2^-. Electron paramagnetic resonance (EPR) spectra indicated that OTIC can produce reactive oxygen species under laser irradiation (Fig. S11D). The photothermal capability of OTIC NPs was continuously monitored for 6 min by using a 660 nm laser (0.5 W/cm²). As depicted in Fig. 2B and Fig. S12 in the ESI, the temperature of OTIC NPs (100 μg/mL) solution increased from 24.3 °C to 55.4 °C, which could cause the apoptosis of tumor cells. Infrared thermal images also confirmed the temperature changes of the OTIC NPs (Fig. S13 in the ESI). The photothermal stability of OTIC NPs (100 μg/mL) was verified in five continuous heating/cooling cycles (Fig. 2C).
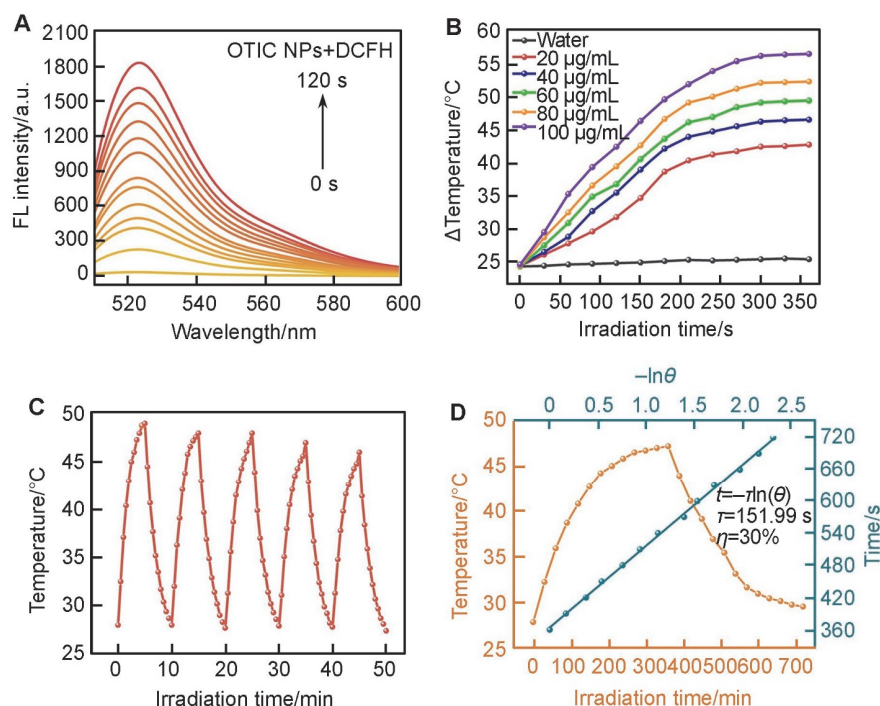

Fig.2 Spectral characterization of OTIC NPs

(A) Time-dependent fluorescent spectra in the presence of DCF (50 mol/L) and OTIC NPs (100 g/mL) under 660 nm laser (0.5 W/cm²) irradiation; (B) temperature variation of OTIC NPs with different concentrations (660 nm, 0.5 W/cm²); (C) temperature elevation by OTIC NPs for five irradiation cycles (660 nm, 0.5 W/cm²); (D) temperature-increasing/decreasing curve and cooling time *vs*. lnθ plot (θ is temperature driving force).

Then a typical heating and cooling cycle of OTIC NPs (100 μg/mL) was recorded with irradiation by 660 nm laser. According to Fig. 2D, the photothermal conversion efficiency was calculated to be 30%, which suggested that OTIC NPs had the potential for photothermal therapy.

3.4 Biocompatibility and Synergistic Tumoricidal Effects of OTIC NPs in Cells

The biocompatibility of OTIC NPs was evaluated with HeLa cells. In Fig. S14A in the ESI, it could be seen that OTIC NPs exhibited red fluorescence in HeLa cells, indicating that OTIC NPs could be uptaken by HeLa cells. Fig. S14B showed the stability of OTIC NPs in PBS solution containing 10% Fetal bovine serum (FBS). It could be observed that after 7 days, the absorbance of OTIC NPs had no obvious change, indicating that the stability of OTIC NPs is good. Before FL/PA dual-modality imaging *in vivo* and the PTT experiment, the cytotoxicity of OTIC NPs (0—80 μg/mL) was investigated by MTT assay. As shown in Fig. 3A and

Fig. S15A in the ESI, OTIC NPs showed almost no toxic effects and cell viabilities remained at 80% even at 80 μg mL. Under the 660 nm laser irradiation, the cell viability decreased with the increase of OTIC NPs concentration. And cell viability remained at 30% at 80 μg/mL (Fig. S15B). Fig. S15C tested the hemolysis rate of OTIC NPs, and it can be seen that at a concentration of 60 μg/mL, the hemolysis rate of cells is still below 5%, indicating that the hemolysis rate of OTIC NPs is relatively low. Calcein AM/PI was applied to distinguishing live (green) and dead (red) HeLa cells (Fig. 3B). The confocal dish was irradiated for 3 min after incubation with OTIC NPs for 4 h. The HeLa cells localized at the laser-irradiating region showed red fluorescence, revealing that most of the cells were dead. While the cells without laser irradiation presented green fluorescence, which indicated that the 4T1 cells were not harmed by the OTIC NPs. The intracellular ROS generation was indicated by DCFH-DA as well. As displayed in Fig. 3C, HeLa cells treated with OTIC NPs aroused bright green fluorescence through NIR laser irradiation, while no obvious fluorescence
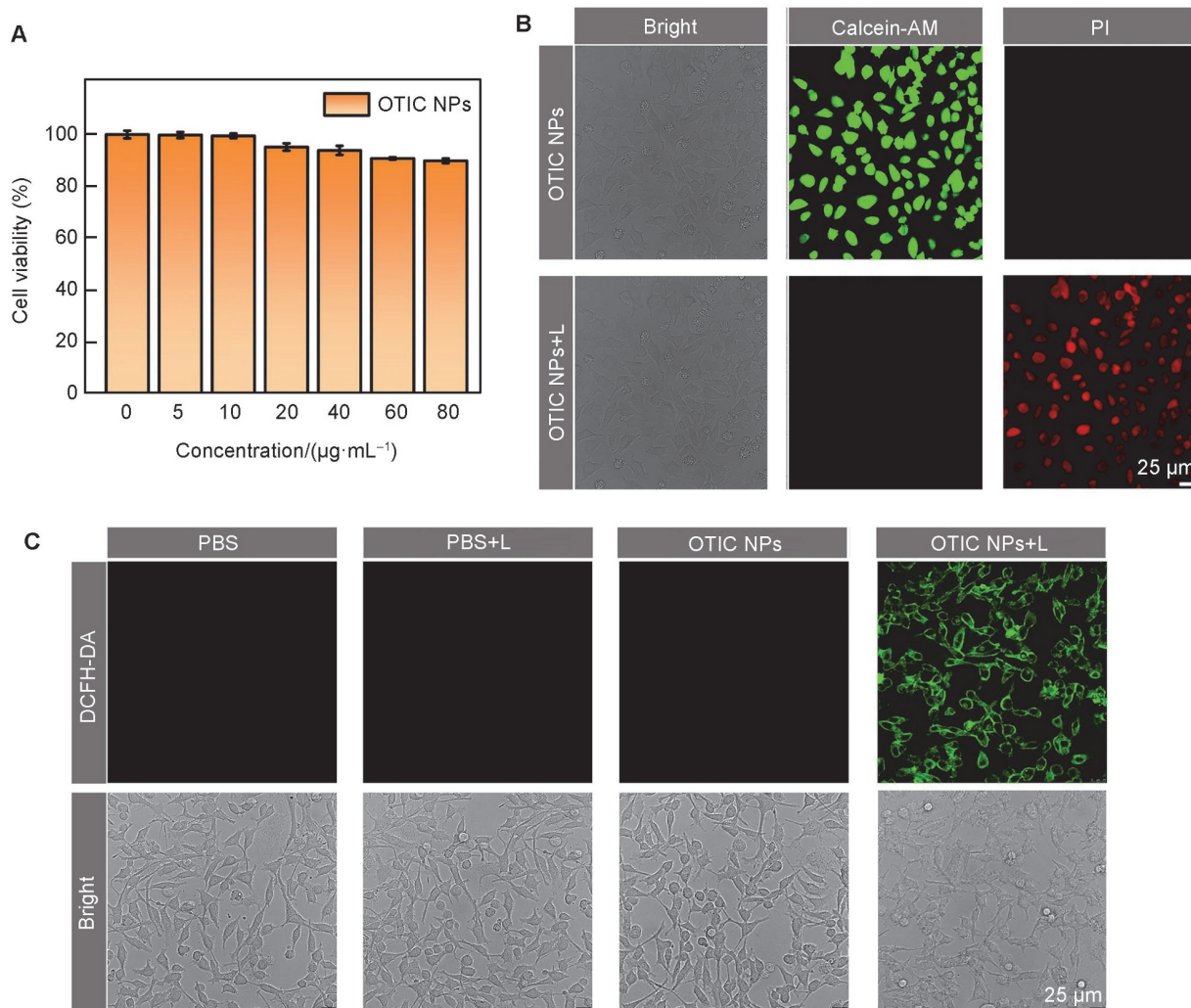

Fig.3 Cell experiments treated with OTIC NPs
(A) Relative cell viabilities of HeLa cells incubated OTIC NPs at various concentrations by MTT method; (B) live/dead HeLa cells staining; (C) intracellular ROS level of HeLa cells treated with DCFH-DA (10 μmol/L).

was observed in the control group. The green fluorescence indicated that ROS could be efficiently generated in cells. The generation of ROS contributed effectively to the high phototoxicity of OTIC NPs against HeLa cells.

3.5 PAI/FLI *In vivo*

To evaluate the capability of OTIC NPs for FL and PA imaging *in vivo*, OTIC NPs were injected into BALB/c mice bearing 4T1 tumors *via* the tail vein. As illustrated in Fig. 4A, at 4 h post-injection, NIR fluorescence signals were subsequently observed in the tumor region, indicating OTIC NPs began to accumulate in the tumor site driven by the EPR effect. The fluorescence signals of the tumor region gradually enhanced and arrived maximum at 6 h post-injection. Then the fluorescence signals became weaker due to the metabolism (Fig. 4, A and B). The fluorescence was still distinguishable at 36 h because of the good retention ability of OTIC NPs in tumor tissues. PA imaging of the tumor region was detected by the MSOT system. As illustrated in Fig. 4, A and C, the PA intensity of the tumor site increased with time elapsing, and reached maximum at 6 h
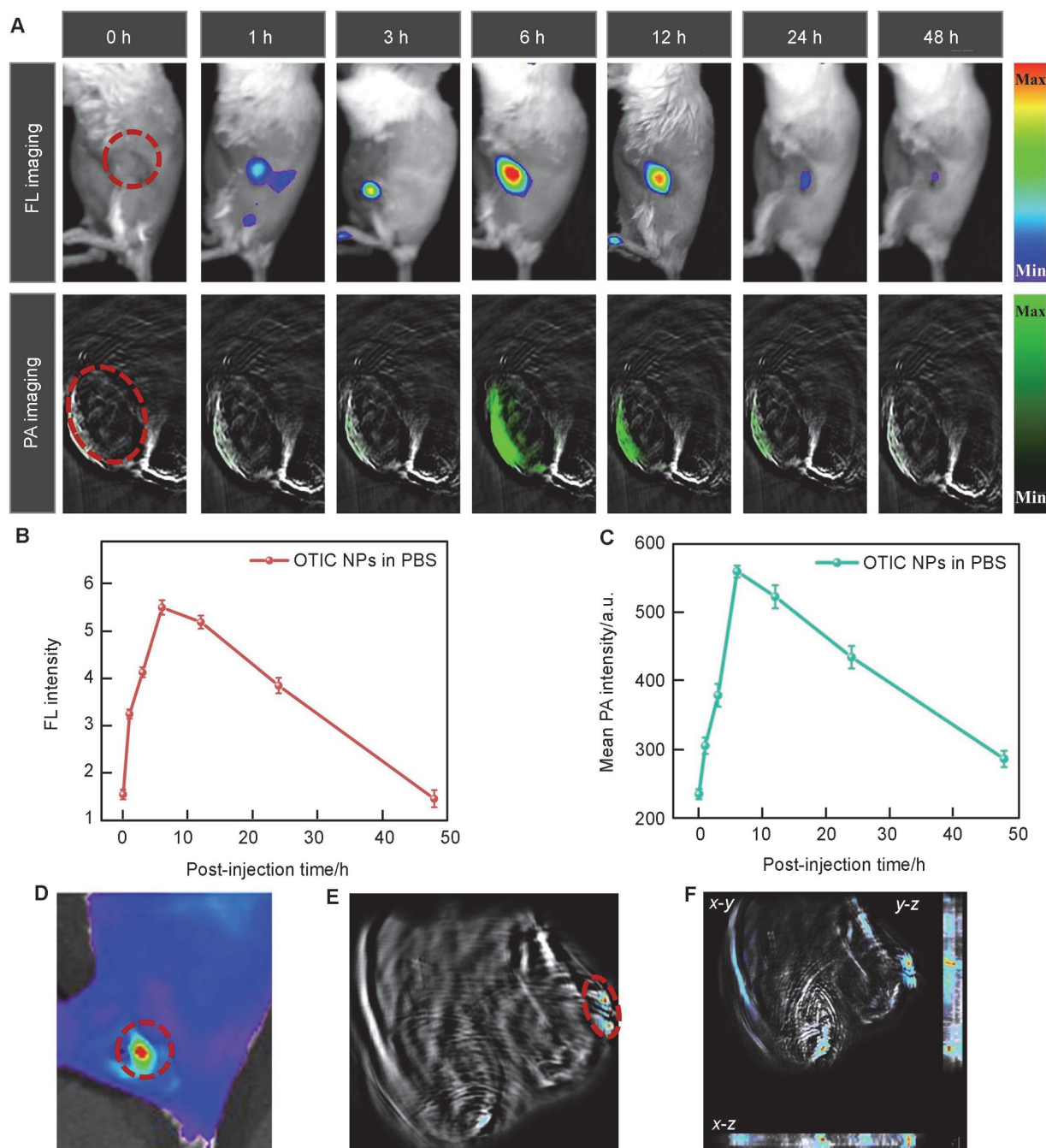

Fig.4 *In vivo* fluorescence and photoacoustic imaging
(A) FL/PA dual-modality images of tumor-bearing mice treated with OTIC NPs; ROI quantified FL (B) and PA intensity (C) of the tumor area at different post-injection time points; fluorescence (D) and photoacoustic imaging (E) of sentinel lymph nodes in left plantar 4T1 tumor-bearing mice; (F) 3D PA image at 2 h post-injection of plantar 4T1 tumor-bearing mice treated with OTIC NPs.

post-injection. The time-dependent trend of PA intensity was coincident with the FL data. OTIC NPs with FLI and PAI provided both good sensitivity and spatial resolution for precise tumor imaging.

The majority of epithelial cancers first develop metastatic growth by spreading *via* lymphatic vessels to their draining lymph nodes (LNs). Some types of malignant tumors, such as breast cancer, melanoma, and prostate cancer are prone to metastasizing to regional LNs, through tumor associated lymphatic channels.[57] The detection of metastases within the sentinel lymph nodes (SLNs) has major prognostic implications for patient survival.[58] Encouraged by the dual-modality imaging of OTIC NPs in the subcutaneous tumor, we performed tumor FL/PA dual-modality imaging of OTIC NPs in mice SLNs. The tumor-bearing mice model was established by injecting 50 μL of 4T1 cells (1×10^7 /mL) in the right hind foot sole of the mice. The mice with a spherical firm lump touchable in their inner knee were used for our experiments after 7 d (Fig. S16 in the ESI). OTIC NPs (2 mg/mL) were injected around the tumor tissue of tumor-bearing mice and FL&PA imaging of SLN was observed at 2 h post-injection. As shown in Fig. 4D, OTIC NPs rapidly aggregated to the SLN tumor site after the injection of OTIC NPs dispersion due to the EPR effect of nanoparticles, and bright fluorescence could be observed in IVIS imaging system in 1 h. Meanwhile, a clear PA signal was also observed in the MSOT system (Fig. 4E). 3D volume reconstruction was performed using multiple cross-sections in the *x*-direction (Fig. 4F). The FL&PA imaging of tumors in mice SLNs further demonstrated the imaging capability of OTIC NPs.

3.6 *In vivo* Dual-modality Imaging-guided Synergistic Treatment by OTIC NPs

As schematically illustrated in Fig. 5A, the orthotopic tumor model was constructed by *in situ* inoculations of *ca.* 1×10^7 4T1 cells in female BALB/c mice. The tumor-bearing mice were intravenously injected with OTIC NPs. In Fig. 4A, the fluorescence and PAI of OTIC NPs peaked at *ca.* 6 h post-injection in the tumor, and OTIC NPs accumulated mostly in the tumor site at 6 h. Therefore, at 6 h post-injection of OTIC NPs, the tumor site was irradiated by a 660 nm laser (0.5 W/cm², 10 min). An infrared thermal camera was used to monitor the change of temperature. The photothermal images and the increasing temperature *versus* exposure time revealed that the temperature of tumor tissue increased rapidly from 34.0 °C to 56.1 °C in 10 min (Fig. 5, B and C). In comparison, the tumor site of PBS-injected mouse presented the negligible temperature change (34.3—38.8 °C) under the same laser irradiation. The tumors of mice treated with OTIC NPs and NIR irradiation were inhibited effectively (Fig. 5D).

The tumors were inhibited completely without any recurrence, only scars remained at day 14 after treatment. The result fully demonstrates the efficacy of OTIC NPs for PTT-PDT synergistic therapy *in vivo* (Fig. 5F). The control groups were settled as OTIC NPs without NIR irradiation and PBS with/without NIR irradiation. The tumor volumes in the control groups increased rapidly and could not be suppressed effectively (Fig. 5D). To evaluate the metabolism of OTIC NPs *in vivo*, mice were sacrificed at various post-injection time points and the main organs were evaluated. As shown in Fig. S17A in the ESI, these organs were imaged with IVIS system. Aided by EPR effects, OTIC NPs first accumulated in the liver and then in the tumor site. The region of interest (ROI) analysis of the FL intensity in different tissues was presented in Fig. 5E. OTIC NPs accumulated mostly in the tumor, and part of OTIC NPs was captured by the liver and spleen. The maximum accumulation was reached at 12 h post-injection. Then the FL intensity of OTIC NPs decreased rapidly in the tumor due to internal metabolism. The mass of the mice in each group did not change too much (Fig. S17B). Hematoxylin and eosin (H&E) staining of tumors showed that "NPs + Laser" group could lead to extensive destruction of tumor tissues, such as abnormal tumor tissues and more cavities (Fig. 5G). The tumor cells in the control groups were numerous and dense. These data indicated that the OTIC NPs could be used as an FL&PA dual-modal imaging-guided phototheranostic agent for blation of tumors *in vivo*.

To investigate the pharmacokinetics of OTIC NPs in living mice after i.v. injection, venous blood samples at various time points were collected to measure the dye contents. Long blood half-life time of 8.09 h for OTIC NPs was obtained (Fig. S18 in the ESI). To investigate the biosafety of OTIC NPs, the serum of mice in every treatment group was collected for a biochemical assay and blood analysis. The biomarkers included alanine aminotransferase (ALT, U/L), aspartate aminotransferase (AST, U/L), serum alkaline phosphatase (ALP, U/L), and albumin (ALB, g/L). The analysis data of experimental mice showed normal hepatic function (Fig. 6A). The whole blood analysis included white blood cells (WBC, 10^9/L), neutrophil granulocytes (Gran, 10^8/L), red blood cells (RBC, 10^{12}/L), hemoglobin (HGB, 10 g/L), hematocrit (HCT, %), mean corpuscular volume (MCV, fL), mean corpuscular hemoglobin concentration (MCHC, 10 g/L), platelets (PLT, 2×10^{11}/L), and mean platelet volume (MPV, 0.1 fL) (Fig. 6B and Fig. S19 in the ESI). The blood data of the mice in the four experimental groups were relatively consistent. White blood cells are the main immune cells that deal with inflammation in mammals. The decrease in white blood cells indicated that the immunity of mice was weak. The stability of other blood data indicated that OTIC NPs and
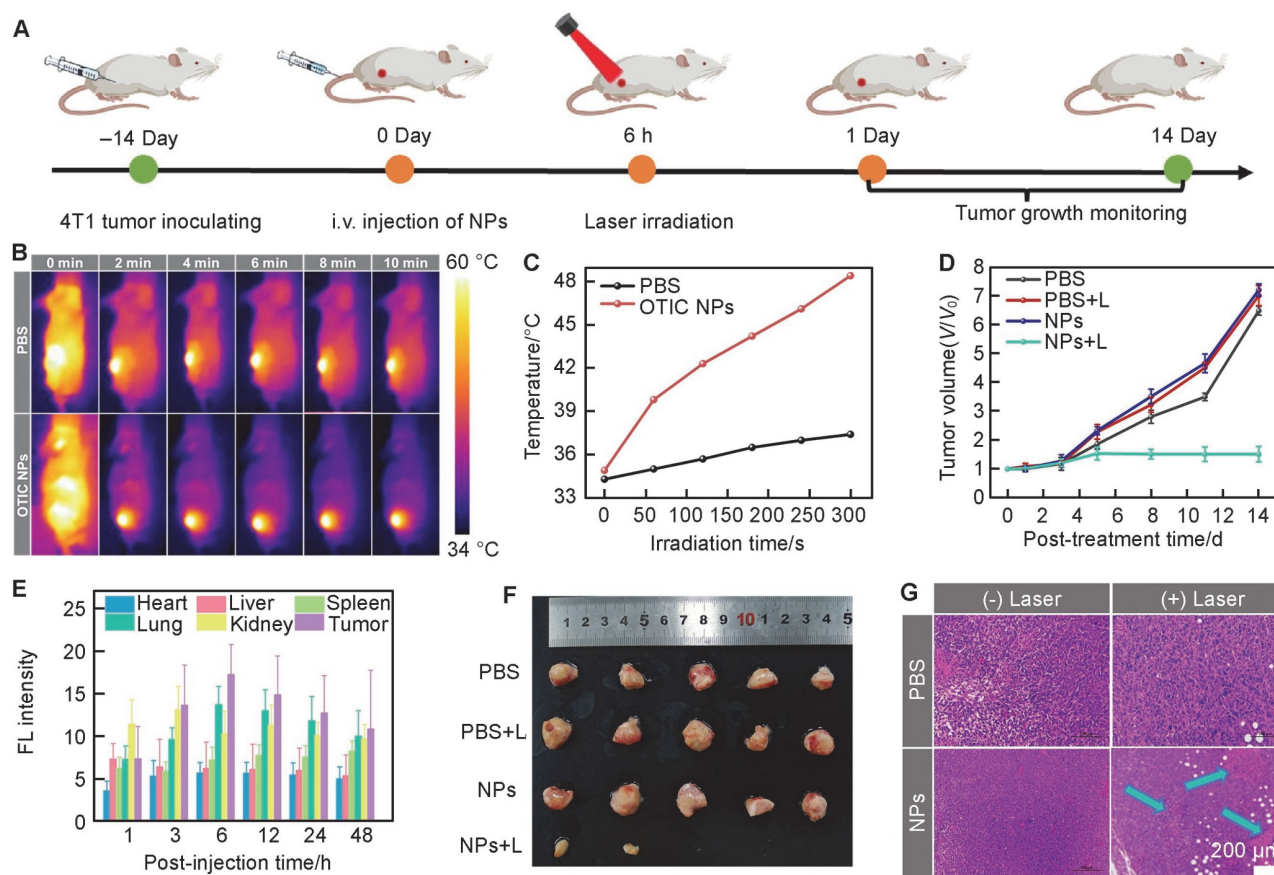
Fig.5 4T1 tumor-bearing mice treated by OTIC NPs

(A) Schematic of schedule for tumor implantation, nanoparticle injection, laser irradiation, and monitoring of tumor growth; (B) infrared thermal images of each group of mice with 660 nm laser (0.5 W/cm^2) irradiation; (C) corresponding statistic temperature changes at the tumor sites during the continuous laser irradiation; (D) time-dependent tumor growth curves of tumor-bearing mice with various treatments (n=5); (E) ROI quantified fluorescence in major organs of mice treated with OTIC NPs at different post-injection time points; (F) representative photographs of the excised tumors 14 d after different treatments applied; (G) H&E staining for tumors on day 14 after different treatments. Scale bar: 200 μm.
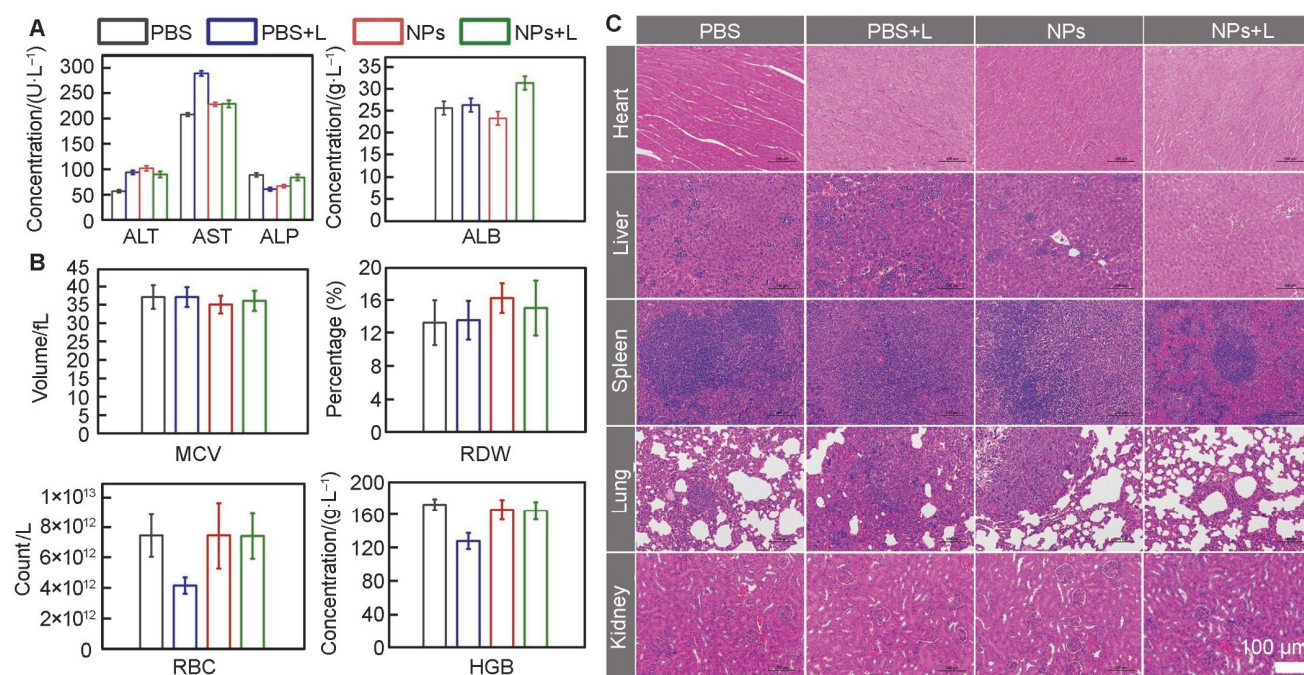

Fig.6 Biosafety evaluation of OTIC NPs

(A) Blood bio-chemistry test regarding the liver function of the mice with and without intravenous injection of OTIC NPs, respectively (n=5 mice for each group); (B) routine blood indexes of the mice with and without intravenous injection of OTIC NPs, respectively (n=5 mice for each group); (C) H&E staining for important organs on day 14 after different treatments.

photothermal therapy did not have adverse effects on the mice. There was no obvious organ damage or inflammatory lesions in the H&E-stained images after treatment with OTIC NPs for 14 d (Fig. 6C).

4 Conclusions

In this study, we synthesized an NIR FL/PA dual-modality imaging agent. OTIC NPs were further used for PTT and PDT of tumors. OTIC NPs presented an S/N ratio of 4.14 in the FL modality. OTIC NPs could be applied for FLI/PAI of mice sentinel lymph nodes sensitively with good spatial resolution. Taking advantage of the intramolecular rotators and vibrators, distorted conformation and high D-A strength of the AIE molecule, OTIC NPs could achieve a balance between radiative and nonradiative excited state energy dissipation. OTIC NPs showed significant NIR fluorescence signals, high ROS generation and 30% of photothermal conversion efficiency upon 660 nm laser irradiation. OTIC NPs had FL/PA imaging and PTT/PDT in single molecular structure, which is due to the suitable electron donor and electron acceptor in OTIC. The multifunction of single molecule would reduce the complex interaction of different molecules in diagnosis and treatment. The multifunctional imaging probe would open up new perspectives on the design of versatile molecular platforms for further application in the clinic field.

Electronic Supplementary Information

Supplementary material is available in the online version of this article at http://dx.doi.org/10.1007/s40242-024-3256-9.

Conflicts of Interest

WANG Zhuo is a youth executive editorial board member for Chemical Research in Chinese Universities and was not involved in the editorial review or the decision to publish this article. The authors declare no conflicts of interest.

References

[1] Chen H., Zhang W., Zhu G., Xie J., Chen X., *Nat. Rev. Mater.*, **2017**, *2*, 17024

[2] Li X., Lovell J. F., Yoon J., Chen X., *Nat. Rev. Clin. Oncol.,* **2020**, *17*, 657

[3] Xu C., Pu K., *Chem. Soc. Rev.,* **2021**, *50*, 1111

[4] Zhang L., Liu Y., Huang H., Xie H., Zhang B., Xia W., Guo B., *Adv. Drug Del. Rev.*, **2022**, *190*, 114536

[5] Li J., Pu K., *Chem. Soc. Rev.,* **2019**, *48*, 38

[6] Cheng H. B., Li Y., Tang B. Z., Yoon J., *Chem. Soc. Rev.*, **2020**, *49*, 21

[7] Ouyang J., Sun L., Zeng F., Wu S., *Coord. Chem. Rev.*, **2022**, *458*, 214438

[8] Ong S. Y., Zhang C., Dong X., Yao S. Q., *Angew. Chem. Int. Ed.,* **2021**, *60*, 17797

[9] Yin X., Cheng Y., Feng Y., Stiles W. R., Park S. H., Kang H., Choi H. S., *Adv. Drug Del. Rev.,* **2022**, *189*, 114483

[10] Chen Y., Chen S., Yu H., Wang Y., Cui M., Wang P., Sun P., Ji M., *Adv. Healthcare Mater.,* **2022**, *11*, 2201158

[11] Xiao Y. F., Xiang C., Li S., Mao C., Chen H., Chen X. H., Tian S., Cui X., Wan Y., Huang Z., Li X., Zhang X. H., Guo W., Lee C. S., *Small*, **2020**, *16*, 2002672

[12] Upputuri P. K., Pramanik M., *Nanomed. Nanobiotechnol.,* **2020,** *12*, e1618

[13] Huang K., Zhang Y., Lin J., Huang P., *Biomater. Sci.,* **2019,** *7*, 472

[14] Du J., Yang S., Qiao Y., Lu H., Dong H., *Biosens. Bioelectron.,* **2021**, *191*, 113478

[15] Zhao Z., Swartchick C. B., Chan J., *Chem. Soc. Rev.,* **2022**, *51*, 829

[16] Ji Y., Jones C., Baek Y., Park G. K., Kashiwagi S., Choi H. S., *Adv. Drug Del. Rev.,* **2020**, *167*, 121

[17] Li C., Chen G., Zhang Y., Wu F., Wang Q., *J. Am. Chem. Soc.,* **2020**, *142*, 14789

[18] Wang X., Guo Z., Zhu S., Liu Y., Shi P., Tian H., Zhu W. H., *J. Mater. Chem. B*, **2016**, *4*, 4683

[19] Shi Y., Zhu D., Wang D., Liu B., Du X., Wei G., Zhou X., *Coord. Chem. Rev.,* **2022**, *471*, 214725

[20] Zhang L., Liu Y., Huang H., Zhang B., Xia W., Guo B., *Adv. Drug Del. Rev.,* **2022**, *190*, 114536

[21] Wang H., Wang Y., Zheng Z., Yang F., Ding X., Wu A., *J. Mater. Chem. B*, **2022**, *10*, 1418

[22] Yang M., Deng J., Su H., Gu S., Zhang J., Zhong A., Wu F., *Mater. Chem. Front.,* **2021**, *5*, 406

[23] Feng L., Li C., Liu L., Wang Z., Chen Z., Yu J., Ji W., Jiang G., Zhang P., Wang J., Tang B. Z., *ACS Nano,* **2022**, *16*, 4162

[24] Chen L., Mao Z., Wang Y., Kang Y., Wang Y., Mei L., Ji X., *Sci. Adv.,* **2022**, *8*, eabo7372

[25] Kang Y., Mao Z., Wang Y., Pan C., Ou M., Zhang H., Zeng W., Ji X., *Nat. Commun.,* **2022**, *13*, 2425

[26] Zhang H., Mao Z., Kang Y., Zhang W., Mei L., Ji X., *Coord. Chem. Rev.,* **2023,** *475*, 214897

[27] Zeng W., Zhang H., Yuan X., Chen T., Pei Z., Ji X., *Adv. Drug Del. Rev.,* **2022**, *184*, 114241

[28] Sai D. L., Lee J., Nguyen D. L., Kim Y. P., *Exp. Mol. Med.,* **2021**, *53*, 495

[29] Huang L., Zhao S., Wu J., Yu L., Singh N., Yang K., Lan M., Wang P., Kim J. S., *Coord. Chem. Rev.,* **2021**, *438*, 213888

[30] Liu X., Liu Y., Li X., Huang J., Guo X., Zhang J., Luo Z., Shi Y., Jiang M., Qin B., Du Y., Luo L., You J., *ACS Nano,* **2022**, *16*, 9240

[31] Li J., Zhang W., Ji W., Wang J., Wang N., Wu W., Wu Q., Hou X., Hu W., Li L., *J. Mater. Chem. B,* **2021**, *9,* 7909

[32] Wang Z., Zhen X., Upputuri P. K., Jiang Y., Pramanik M., Pu K., Xing B., *ACS Nano,* **2019**, *13*, 5816

[33] Moses A. S., Taratula O. R., Lee H., Luo F., Grenz T., Korzun T., Lorenz A. S., Sabei F. Y., Bracha S., Alani A. W. G., Slayden O. D., Taratula O., *Small,* **2020**, *16*, 1906936

[34] Wang J., Liu Y., Morsch M., Lu Y., Shangguan P., Han L., Wang Z., Chen X., Song C., Liu S., Shi B., Tang B. Z., *Adv. Mater.,* **2022**, *34*, 2106082

[35] Zhang L., Zhuang W., Yuan Y., Shen J., Shi W., Liu G., Wu W., Zhang Q., Shao G., Mei Q., Fan Q., *ACS Appl. Mater. Interfaces,* **2022**, *14*, 24174

[36] Zhang Z., Xu W., Kang M., Wen H., Guo H., Zhang P., Xi L., Li K., Wang L., Wang D., Tang B. Z., *Adv. Mater.,* **2020**, *32*, 2003210

[37] Yin B., Qin Q., Li Z., Wang Y., Liu X., Liu Y., Huan S., Zhang X., Song G., *Nano Today,* **2022**, *45*, 101550

[38] Chen C., Ou H., Liu R., Ding D., *Adv. Mater.,* **2020**, *32*, 1806331

[39] Feng G., Zhang G. Q., Ding D. *Chem. Soc. Rev.,* **2020**, *49*, 8179

[40] Jin Z. Y., Fatima H., Zhang Y., Shao Z., Chen X. J., *Adv. Therap.,* **2022**, *5*, 2100176

[41] Ding G., Tong J., Gong J., Wang Z., Su Z., Liu L., Han X., Wang J., Zhang L., Wang X., Wen L. L., Shan G. G., *J. Mater. Chem. B,* **2022**, *10*, 5272

[42] Cheng K., Chen H., Jenkins C. H., Zhang G., Zhao W., Zhang Z., Han F., Fung J., Yang M., Jiang Y., Xing L., Cheng Z., *ACS Nano,* **2017**, *11*, 12276

[43] Shao W., Wei Q., Wang S., Li F., Wu J., Ren J., Cao F., Liao H., Gao J., Zhou J., Ling D., *Mater. Horiz.,* **2020**, *7*, 1379

[44] Gao H., Duan X., Jiao D., Zeng Y., Zheng X., Zhang J., Ou H., Qi J., Ding D., *Angew. Chem. Int. Ed.,* **2021**, *60*, 21047

[45] Li X., Zhang D., Yin C., Lu G., Wan Y., Huang Z., Tan J., Li S., Luo J., Lee C. S., *ACS Appl. Mater. Interfaces,* **2021**, *13*, 15983

[46] Mei J., Hong Y., Lam J. W.Y., Qin A., Tang Y., Tang B. Z., *Adv. Mater.,* **2014**, *26*, 5429

[47] Yan D., Xie W., Zhang J., Wang L., Wang D., Tang B. Z., *Angew. Chem. Int. Ed.,* **2021**, *60*, 2

[48] Liu L., Wang X., Wang L. J., Guo L., Li Y., Bai B., Fu F., Lu H., Zhao X., *ACS Appl. Mater. Interfaces,* **2021**, *13*, 19668

[49] Zhang C., Yuan J., Ho J. K. W., Song J., Zhong H., Xiao Y., Liu W., Lu X., Zou Y., So S. K., *Adv. Funct. Mater.,* **2021**, *31*, 2101627

[50] Yang Y., Liu Z., Zhang G., Zhang X., Zhang D., *Adv. Mater,* **2019**, *31*, 1903104

[51] Sabouri S., Liu M., Zhang S., Yao B., Soleimaninejad H., Baxter A. A., Vidales G. A., Subedi P., Duan C., Lou X., Hogan C. F., Heras B., Poon I. K. H., Hong Y., *Adv. Health. Mater,* **2021**, *10*, 2101300

[52] Kim C., Song K. H., Gao F., Wang L. V., *Radiology,* **2010**, *255*, 442

[53] Xu R., Jiao D., Long Q., Li X., Shan K., Kong X., Ou H., Ding D., Tang Q., *Biomaterials,* **2022**, *289*, 121780

[54] Fathi P., Knox H. J., Sar D., Tripathi I., Ostadhossein F., Misra S. K., Esch M. B., Chan J., Pan D., *ACS Nano,* **2019**, *13*, 7690

[55] Mu X., Feng W., Li C., Li K., Li Y., Jing X., Lu Y., Zhou X., Li Z., *Anal. Chem.,* **2022**, *94*, 9775

[56] Cho S., Lee J., Tong M., Seo J. H., Yang C., *Adv. Funct. Mater.,* **2011**, *21*, 1910

[57] Niu G., Chen X., *Theranostics,* **2015**, *5*, 686

[58] Karaman S., Detmar M., *J. Clin. Invest.,* **2014**, *124*, 922